Available online at www.sciencedirect.com

ScienceDirect

Procedia Structural Integrity 28 (2020) 2267–2276

Structural Integrity Procedia

www.elsevier.com/locate/procedia

1st Virtual European Conference on Fracture

Calibrating a ductile damage model for two pipeline steels: method and challenges

Robin Depraetere[a,*], Margo Cauwels[b], Wim De Waele[a], Tom Depover[b], Kim Verbeken[b], Stijn Hertelé[a]

[a]*Ghent University, Department of Electromechanical, Systems and Metal Engineering, Soete Laboratory, Technologiepark-Zwijnaarde 46, 9052 Zwijnaarde, Belgium*

[b]*Ghent University, Department of Materials, Textiles and Chemical Engineering, Sustainable Materials Science, Technologiepark-Zwijnaarde 46, 9052 Zwijnaarde, Belgium*

Abstract

This work is part of a project that aims to develop a micromechanics based damage law taking into account hydrogen assisted degradation. A 'vintage' API 5L X56N and a 'modern' API 5L X70M pipeline steel have been selected for this purpose. The paper focuses on an experimental calibration of ductile damage properties of the well known complete Gurson model for the two steels in absence of hydrogen. A basic microstructural characterization is provided, showing a banded ferrite-pearlite microstructure for both steels. Charpy impact tests showed splits at the fracture surface for the X70 steel. Double-notched round bar tensile tests are performed, aiming to provide the appropriate input for damage model calibration. The double-notched nature of the specimens allows to examine the material state at maximum load in the unfailed notch, and the final material state in the failed notch. Different notch radii are used, capturing a broad range of positive stress triaxialities. The notches are optically monitored for transverse necking in two perpendicular directions (transverse to rolling and through thickness) to reveal any anisotropy in plastic deformation and/or damage. It is explained how the occurrence of splits at the segregation zone, and anisotropy complicate the calibration procedure. Calibration is done for each steel and acceptable results are obtained. However, the occurrence of splits did not allow to evaluate the damage model for the highest levels of tested stress triaxiality.

Keywords: Complete Gurson model; Pipeline steel; Notched round bar; Splits; Anisotropy

1. Introduction

Hydrogen gas as an energy carrier is key in the transition towards a low-carbon economy, necessary in reducing global warming [H2Europe (2020)]. Pipeline systems are used as an economical means for storing and transporting

* Corresponding author.
E-mail address: robidpra.Depraetere@UGent.be

2452-3216
10.1016/j.prostr.2020.11.072

energy, potentially in the form of hydrogen gas. However, it is well known that hydrogen build-up in steel reduces its ductility and toughness, and promotes cracking [Gangloff and Somerday (2012)]. This phenomenon is widely acknowledged as hydrogen embrittlement. Accordingly, the effect of hydrogen on the mechanical behavior of pipeline steel is extremely relevant, in order to give guidance in assessing the safety of a pipeline structure.

To this purpose, a micromechanics based damage model will be developed including hydrogen assisted degradation. The intention is to calibrate the numerical damage model using tensile tests on both uncharged and hydrogen charged specimens. Fracture toughness tests will be performed to characterize the hydrogen assisted degradation of the tearing resistance. Two pipeline steels have been selected, each manufactured using a different production process, suggesting a difference in mechanical behavior, and in susceptibility to hydrogen embrittlement.

The first step in developing the model is characterizing the mechanical behavior of both steels in the absence of hydrogen. This paper reports the framework and the results for the calibration of a ductile damage model for both steels. The employed damage model is the complete Gurson model [Zhang et al. (2000); Su et al. (2020)] and should be able to predict the onset of failure. It is discussed how two observed material effects (i.e. split occurrence and plastic anisotropy) may complicate the calibration procedure of the model parameters. Finally, calibration is performed for both steels and the optimal model parameters are obtained.

2. Materials characterization

Two pipeline steels that had been in service for numerous years have been selected. The first material is a grade API 5L X56N and was produced in 1965 by a normalized rolling process. The pipe from which specimens are extracted has an outside diameter of 914.4mm (36”) and a measured wall thickness of around 15.5mm. The second material has grade API 5L X70M and was produced in 1991 by a thermomechanically controlled process (TMCP). The pipe has an outside diameter of 1016mm (40”) and a measured wall thickness of 15.8mm. Both pipes have a longitudinal seam weld. The two materials are further referred to as ‘X56’ and ‘X70’ respectively.

The constitutive behavior was characterized by means of uniaxial tensile tests in the longitudinal (L) direction, according to ISO 6892-1 (2016). To provide statistical reliability, three tests were performed for each material. The specimens were extracted with a rectangular cross-section covering most of the wall thickness. Table 1 summarizes the key values characterizing yielding, plasticity and ductility; the yield strength $R_{t0.5}$, the tensile strength R_m, the yield to tensile strength ratio $R_{t0.5}/R_m$, and the elongation at fracture A. A larger strain hardening (indicated by the smaller yield to tensile ratio) and a larger ductility is observed for the X56 steel.

Table 1: Tensile properties of the investigated pipeline steels (longitudinal to pipe axis). Average and standard deviation based on three tests is reported.

Pipeline steel grade	$R_{t0.5}$ [MPa]	R_m [MPa]	$R_{t0.5}/R_m$ [-]	A [%]
API 5L X56N	391 ± 3	579 ± 2	0.68 ± 0.004	27.4 ± 1.0
API 5L X70M	508 ± 4	614 ± 1	0.83 ± 0.004	20.2 ± 0.2

The chemical composition of both materials is given in Table 2. The X56 steel has a larger carbon content than the more modern X70 steel, and contains more impurities in the form of sulfur and phosphorus. A basic microstructural characterization is provided by means of light optical microscopy (LOM) in all three principal planes. In Figure 1 a heterogeneous microstructure in the form of alternating ferrite-pearlite layers can be noticed, which is typical for these steels. A grain size analysis in the transversal plane according to the Heyn lineal intercept method [ASTM E112 (2010)] resulted in an equivalent average ferritic grain size diameter of 7.2 μm and 3.9 μm for the X56 and X70 steel, respectively.

Charpy V-notch specimens were extracted with their longest direction and the crack propagation path in the longitudinal (L) and the transversal (T) direction of the pipe, respectively, according to ASTM E23 (2007). The average Charpy V-notch impact energy obtained at room temperature was 70 J and 177 J for the X56 and X70 steel, respectively. Furthermore, it must be noted that severe splits could be observed on the fracture surface of all X70 specimens, with the most severe occurrence for the lowest temperature, visible in Figure 2. The separations occurred perpendicular to the fracture face and parallel to the crack propagation direction. This type of separation is often refered to as

Table 2: Chemical composition of the investigated pipeline steels in weight percentage.

Pipeline steel grade	C	Mn	Si	Cr	Ni	Nb	V	Mo	Cu	S	P
API 5L X56N	0.230	1.392	0.364	0.067	0.062	0.002	0.002	0.022	0.122	0.036	0.024
API 5L X70M	0.108	1.633	0.426	0.030	0.022	0.054	0.068	0.002	0.018	0.003	0.015

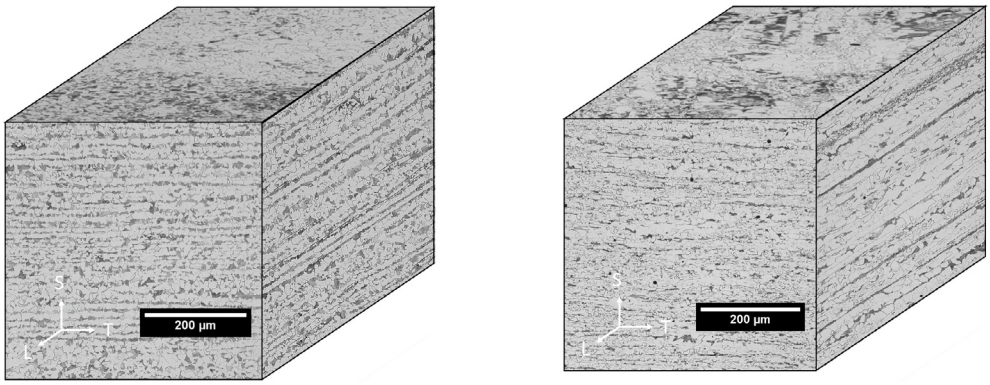

(a) X56 (b) X70

Fig. 1: The microstructure in the longitudinal (L), transversal (T) and through-thickness (S) direction, assessed using LOM of the (a) X56 steel and (b) X70 steel

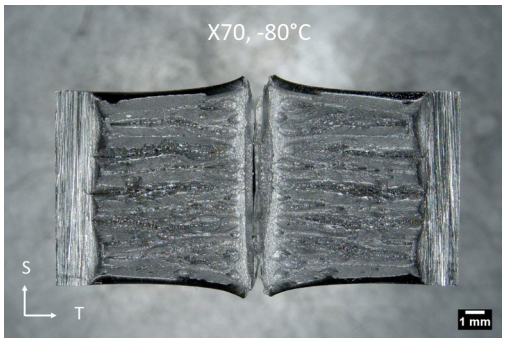

Fig. 2: Fracture surface of Charpy specimen of X70 material at lowest test temperature (-80°C). The crack-divider type of split is evident.

crack-divider type in literature [Haskel et al. (2014); Ruggieri and Hippert Jr. (2015); Davis (2017)]. Accordingly, the splits run corresponding to the alternating banded ferrite-pearlite microstructure, in the transversal (T) direction.

3. Experimental framework

3.1. Specimen geometry

Calibrating the complete Gurson damage model will be done based on the matching of experimental load-deformation curves resulting from tensile tests, with numerical load-deformation curves from simulations. Different specimen geometries have to be employed, in order to obtain different stress triaxialities. Standard smooth round bar specimens and double-notched round bars were manufactured according to Figure 3. Note that the minimum cross-sectional diameter of the notched round bars is also equal to 6mm.

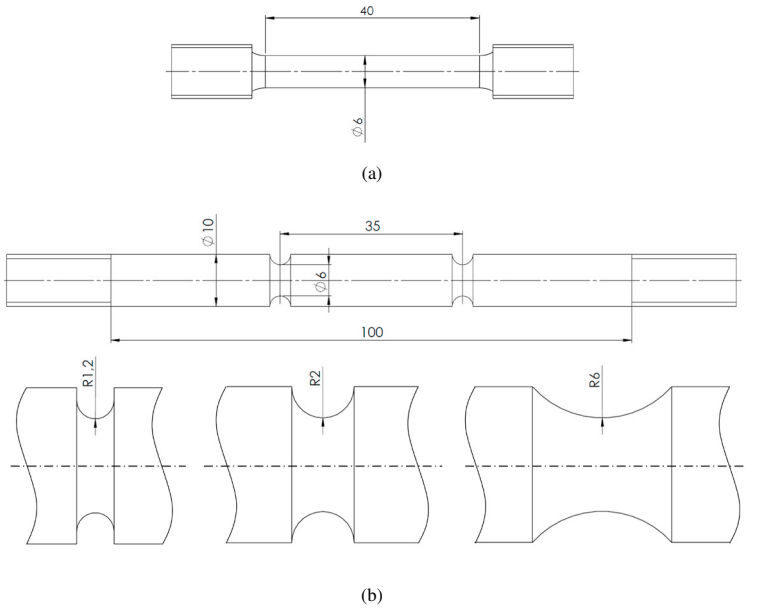

Fig. 3: Specimen geometry of (a) the smooth round bars and (b) the double-notched round bars

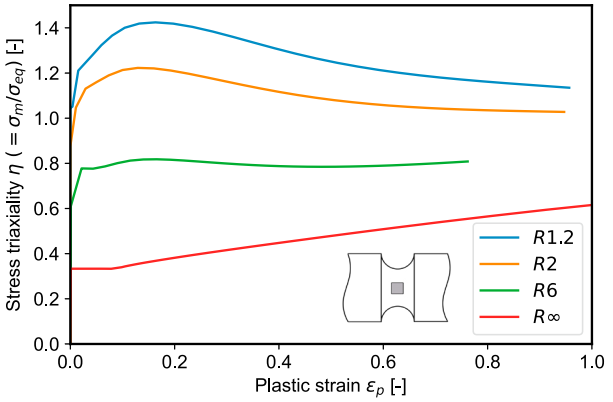

Fig. 4: Stress triaxiality values extracted from the central element of a notched specimen

The use of two notches was proposed by Kim et al. (2018). The idea is that both notches will behave similar up to maximum load, after which one notch starts necking while the other begins to unload elastically. This type of specimen allows two damage states to be investigated microscopically after testing, one of which is the state at maximum load.

The notched specimens were designed with three different notch radii, R = 1.2mm, 2mm and 6mm. A preliminary finite element (FE) study indicated that these radii cover a broad range of positive triaxiality values. Figure 4 shows the evolution of triaxiality as a function of the plastic strain, obtained at the center element of the notched region where the highest triaxiality can be found. With decreasing notch radius, the stress triaxiality attained at the center of the specimen increases. Note that the smooth specimen is denoted with $R\infty$, and that its stress triaxiality at small scale yielding conditions attains the theoretical value of 1/3 for uniaxial loading.

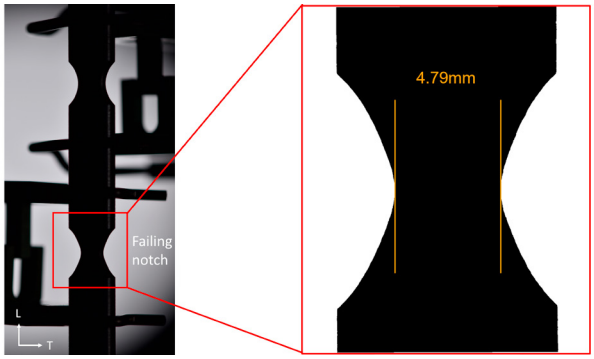

Fig. 5: Diameter reduction during the test for a double-notched R6 specimen (illustration for material X56)

3.2. Experimental method

During the tensile test, the deformation of the notch must be measured. Since it is uncertain to know a priori which notch will fail, an extensometer is positioned over each notch, measuring the axial elongation. The lateral contraction of the notch was monitored optically using regular digital single-lens reflex (DSLR) cameras. The cameras were triggered at a fixed frequency such that about 100 pictures per test were anticipated. Lighting conditions were tuned to obtain a high-contrast picture. This facilitates the extraction of the edge of the specimen, and thus the diameter contraction. To allow the evaluation of potential anisotropy of both steels, two cameras were positioned perpendicularly, observing the contraction in both the transverse (T) and the through-thickness (S) direction.

The pictures were processed using *Python (3.8)* and *ImageJ (1.53c)* by applying a brightness threshold. Figure 5 illustrates the result of the postprocessing algorithm for a specimen with notch R6. The original picture is presented on the left, and on the right the thresholded image and the calculated diameter are demonstrated. As a result of the high contrast between the specimen and the background, the sensitivity of the selected brightness threshold on the resulting diameter is limited.

4. Experimental results

4.1. Force-displacement

Figure 6 provides the force F versus the axial elongation ΔL extracted from the extensometer positioned at the failed notch. The tensile test data for the smooth bar from the X56 steel does not go till fracture, since necking occurred close to the extensometer legs. The figure shows that the maximum force increases with decreasing notch radius, while the elongation decreases. This is explained by the increased triaxiality with a decreasing notch radius [Oh et al. (2007)].

Interesting is that the tensile results for the specimens with notch R1.2 of both steels and notch R2 of X56 do not show smooth behavior in the plasticity region. A rather sudden drop in the force is observed, indicating that the specimen abruptly loses load-carrying capacity. Fractography of the R1.2 notch of the X70 steel showed the occurrence of a split along the transversal direction, similar to the Charpy tests (Figure 7). In addition, Figure 7(b) shows that the split took place in the highly-banded, impure segregation region, at the center of the specimen. The cause of the split is believed to be the occurrence of a high normal stress in the through-thickness direction at the center of the specimen, combined with a weak interface between adjacent layers at the segregation zone. The fracture surface of the X56 specimens showed less severe splits, yet separation happened there as well along the pearlite-ferrite layered structure.

It is apparent that the occurrence of these sudden drops in force will pose a significant challenge with respect to calibrating the damage model. First of all, the ductile damage model is unable to model the brittle-like separation between the different layers. Moreover, the high triaxiality obtained at the center of the specimen drops upon separation.

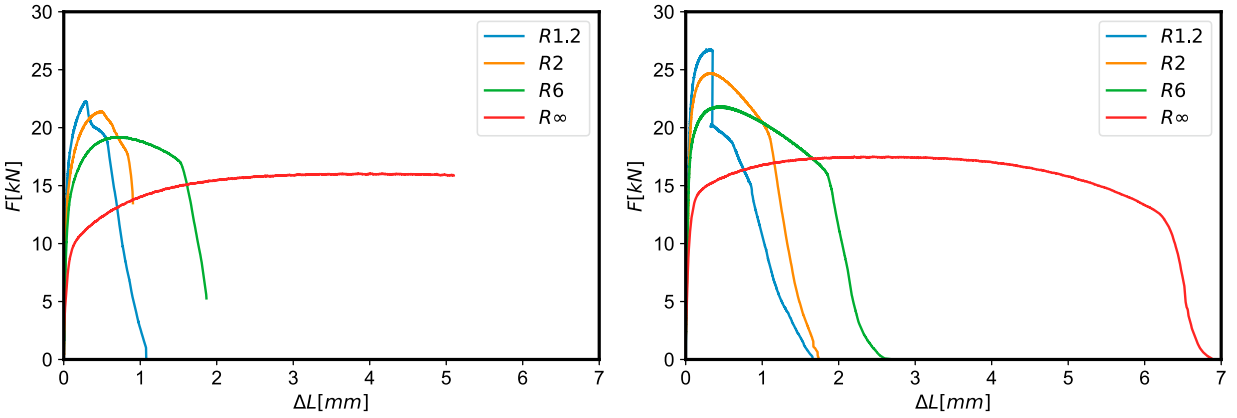

(a) X56 (b) X70

Fig. 6: The force F versus axial displacement ΔL for (a) X56 steel and (b) X70 steel

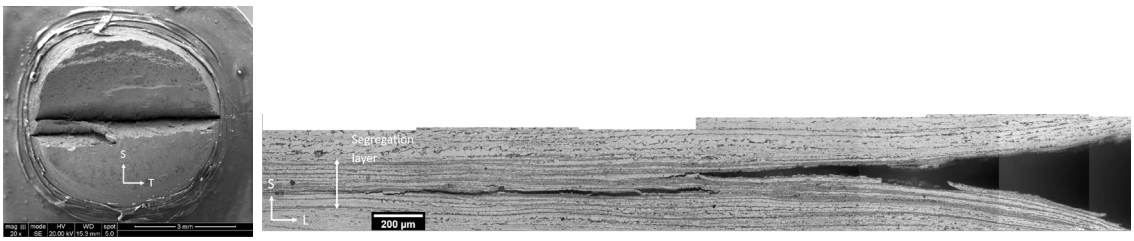

(a) (b)

Fig. 7: Observed split for R1.2 specimen, material X70 in the (a) L-plane and (b) T-plane

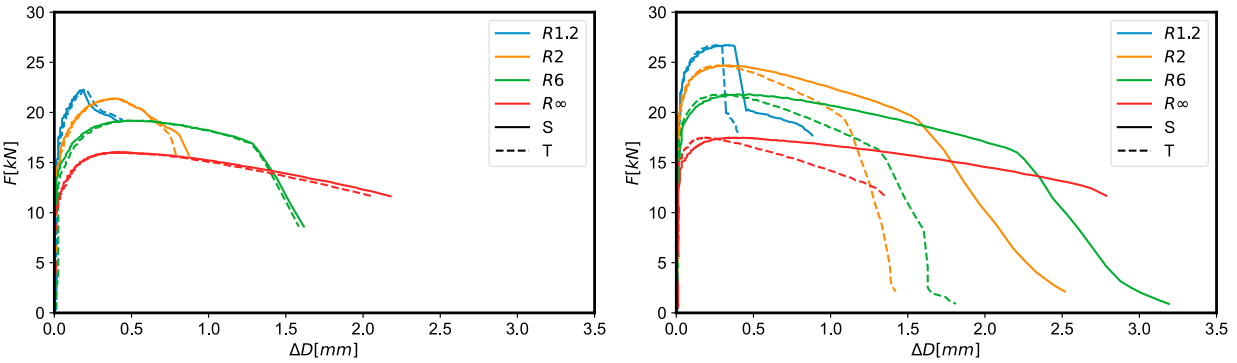

(a) X56 (b) X70

Fig. 8: The force F versus lateral diameter contraction ΔD for (a) X56 steel and (b) X70 steel. The contractions in the through-thickness (S) direction and the transverse (T) direction are shown by the full and the dotted line respectively.

4.2. Force-contraction

Besides the axial displacement, the lateral deformation of the notch is employed to calibrate the damage model. By correlating the processed pictures with the corresponding force, the diameter contraction as a function of load in both the S and the T direction can be obtained. The results are presented in Figure 8.

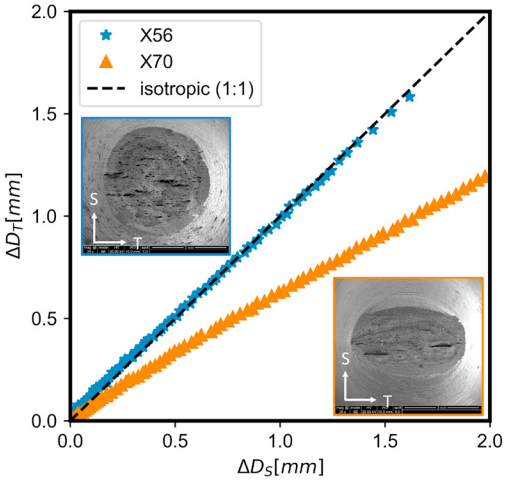

Fig. 9: Comparison of the diameter contraction ΔD in both directions for both steels for a specimen with notch R6

First of all, the occurrence of splits is also visible in Figure 8. In addition, the difference in diameter contraction ΔD between the through-thickness (S) and the transversal (T) direction is interesting. For the X56 steel, no significant difference can be observed, indicating macroscopic isotropic behavior. However, the X70 steel results reveal significant plastic anisotropy. The comparison of lateral contraction in both directions is shown in Figure 9 for both steels, for a specimen with notch R6. Also, the fracture surfaces of both specimens are given. Note that, although the X56 steel exhibits macroscopic isotropic behavior, small splitting cracks parallel to the transverse direction can be observed. The presence of plastic anisotropy for the X70 steel results in an additional challenge for calibrating the damage model.

5. Damage model calibration

5.1. Complete Gurson model

The numerical ductile damage model that will be used is the complete Gurson model (CGM) [Zhang et al. (2000)]. It is micromechanically based, and therefore describes the complete ductile fracture process, including void nucleation, growth and coalescence. The advantage of CGM over other Gurson-type models, is that the critical void volume fraction f_c is not a material constant in CGM, but depends on the local stress and strain fields through Thomason's plastic limit load model [Younise et al. (2017)].

The model assumes that each element has a certain void volume fraction f, specifying the evolution of damage. An initial void volume fraction f_0 is assigned, and complete failure occurs when f reaches the final void volume fraction f_f. The complete Gurson model consists out of the constitutive equation of Gurson-Tvergaard & Needleman (GTN), complemented by the void coalescence criterion of Thomason [Zhang et al. (2000)]:

$$\phi(\boldsymbol{\sigma}, \bar{\sigma}, f^*) = \left(\frac{\sigma_e}{\bar{\sigma}}\right)^2 + 2q_1 f^* \cosh\left(\frac{3q_2\sigma_h}{2\bar{\sigma}}\right) - 1 - q_3 f^{*2} = 0 \tag{1}$$

$$\frac{\sigma_1}{\bar{\sigma}} = \left(\alpha\left(\frac{1}{r} - 1\right)^2 + \frac{\beta}{\sqrt{r}}\right)(1 - \pi r^2) \tag{2}$$

Equation 1 gives the constitutive GTN yield criterion with $\boldsymbol{\sigma}$ the stress tensor, $\bar{\sigma}$ the current flow stress, f^* the effective void volume fraction, σ_e the von Mises stress, σ_h the hydrostatic stress, and q_1, q_2, q_3 empirical constants. Equation 2 presents the criterion for void coalescence to occur. In this equation, σ_1 is the current maximum principal

stress, r the void space ratio defined as $r = \sqrt[3]{(3f/4\pi)e^{\epsilon_1+\epsilon_2+\epsilon_3}}/(\sqrt{e^{\epsilon_2+\epsilon_3}}/2)$, ϵ_i the principal logarithmic strains and α, β constants. In order to improve the numerical effect of coalescence, the void volume fraction f is artificially accelerated upon coalescence and is represented by the effective void volume fraction f^* [Zhang et al. (2000)].

The increase in void volume fraction $\dot{f}$ is governed by the sum of two contributions: the growth of existing voids $\dot{f}_{growth}$ and the nucleation of new voids $\dot{f}_{nucleation}$. Void growth can be derived from mass conservation as $\dot{f}_{growth} = (1-f)\dot{\epsilon}^p_{kk}$, with $\dot{\epsilon}^p_{kk}$ the trace of the plastic strain rate tensor. Void nucleation is based on the strain-controlled approach proposed by Chu and Needleman (1980):

$$\dot{f}_{nucleation} = \frac{f_N}{s_N\sqrt{2\pi}} \exp\left\{-\frac{1}{2}\left[\frac{\epsilon^p_{eq} - \epsilon_N}{s_N}\right]^2\right\}\dot{\epsilon}^p_{eq} \tag{3}$$

with ϵ^p_{eq} the equivalent plastic strain, f_N the void volume fraction of void nucleating particles, s_N and ϵ_N the standard deviation and the mean nucleating strain respectively.

5.2. Calibration procedure

The complete Gurson model consists in total of eight parameters ($\epsilon_N, s_N, f_N; f_0, f_f; q_1, q_2, q_3$) that need to be calibrated for a given material. Typically, these parameters are obtained through a combination of literature identification and matching numerical simulations with experimental results of tensile tests using specimens with varying stress triaxialities. The calibration process may be assisted by metallurgical investigations or chemical analysis, aimed at quantifying the initial void volume fraction. It is common to select parameters $\epsilon_N, s_N, q_1, q_2, q_3$ based on available literature, and to fit the remaining parameters f_N, f_0, f_f to obtain the closest match with the experimental results [Rahimidehgolan et al. (2017)]. This approach is adopted in the present work. Five parameters are fixed to typical values suggested in literature [Rahimidehgolan et al. (2017); Oh et al. (2007)]: $\epsilon_N = 0.3, s_N = 0.1, q_1 = 1.5, q_2 = 1.0, q_3 = 2.25$. An objective function is constructed, representing the difference between the experimental and numerical force-elongation and force-diameter reduction curves, in the form of the root mean square error (RMSE). The RMSE regarding the elongation and the contraction are summed up, and the objective function is obtained. Finally, the optimal parameter set f_N, f_0, f_f is obtained by selecting the minimal objective function.

The results of the tensile tests revealed two significant challenges that must be dealt with: occurrence of splits and plastic anisotropy. Regarding anisotropy, the most pragmatic approach is to calibrate the model using the average diameter contraction $(\Delta D_S + \Delta D_T)/2$, effectively ignoring the anisotropic behavior present in the material. A more rigorous alternative would be to explicitly include plastic anisotropy into the numerical damage model. For example, Hill's anisotropic yield criterion might be implemented [Hill (1998); Rivalin et al. (2001)]. The explicit modelling of anisotropic plasticity requires more tensile tests in different directions to capture the anisotropic behavior properly, and is therefore not preferred in this work. Concerning splits, the adopted approach is to exclusively use the part of the load-deformation curves before the occurrence of a split. This approach is very simple, but the disadvantage is that mainly plasticity with only limited damage is taken into account for the high-triaxiality specimens. An alternative could be to explicitly model the split that was observed in the experimental tensile tests, for example by combining cohesive zone elements modelling separation, and Gurson elements modelling the ductile crack propagation. This approach has already been successfully employed to model splits in Charpy impact tests [Davis (2017)].

5.3. Results

The optimal parameter set for both materials is provided in Table 3. The experimental and numerical force-elongation and force-contraction curves are presented in Figure 10. Note that the data of the experimental curves used for calibration (i.e. before split occurrence) is represented by full circles. Furthermore, the averaged diameter contraction is set out, since this quantity is used for the calibration. It is apparent from the graphs that a good fit between the simulations and the experiments is obtained. This suggests that the approaches selected for dealing with the observed material effects might be adequate for our specific research goals, a hypothesis that will be investigated in further work.

Table 3: Calibrated damage model parameters of the complete Gurson model (CGM) for both pipeline steels

Pipeline steel	ϵ_N	s_N	f_N	f_0	f_f	q_1	q_2	q_3
X56	0.3	0.1	0.0299	0.00189	0.376	1.5	1.0	2.25
X70	0.3	0.1	0.0160	0.00012	0.446	1.5	1.0	2.25

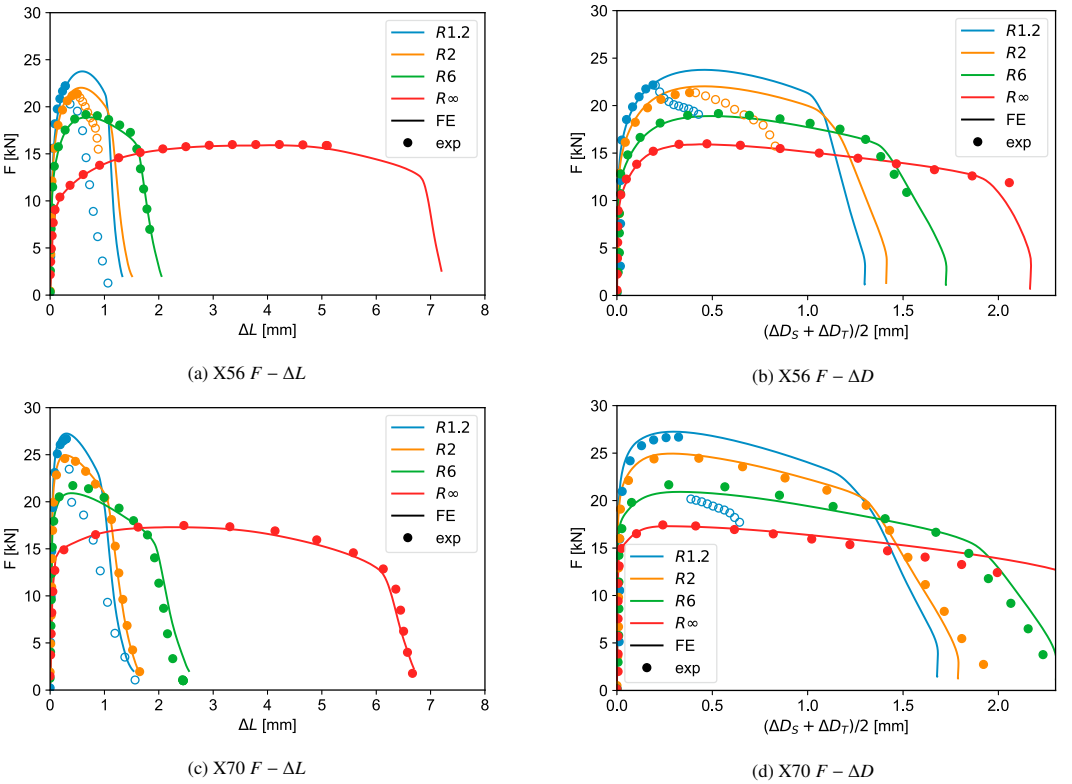

(a) X56 $F - \Delta L$

(b) X56 $F - \Delta D$

(c) X70 $F - \Delta L$

(d) X70 $F - \Delta D$

Fig. 10: Comparison between experimental and numerical finite element (FE) load-elongation ($F - \Delta L$) and load-contraction ($F - \Delta D$) curves for both investigated steels. The experimental data used for calibration is represented by full circles.

6. Conclusions

This paper presents a method to calibrate the complete Gurson model (CGM) for two pipeline steels (API 5L X56 and API 5L X70). Both steels show a heterogeneous microstructure, consisting of alternating ferrite-pearlite layers. Material characterization by means of tensile tests and Charpy impact tests established the differences in behavior of both materials. Splits could be observed on the fracture surface of the Charpy specimens of the X70 steel. Tensile tests on double-notched round bars and smooth round bars achieved a broad range values of stress triaxialities. During the test, the axial elongation is measured, and the lateral contraction in two directions at the notch is monitored optically. The deformation data from the tensile tests reveals two major challenges with respect to the calibration of the model. Firstly, splits manifested by a sudden force drop and a sharp crack were observed in both steels, for the geometries with the sharpest notch. A preliminary microstructural investigation showed that the split propagated along the banded ferrite-pearlite layers, and occurred in the segregation zone of the pipe. Since a ductile damage model cannot incorporate the brittle-like concept of a split, the current study discarded the experimental data after split occurrence. Secondly, from the analysis of the lateral diameter contraction in different directions it can be concluded that the X70 steel shows notable anisotropic plasticity, unlike the macroscopically isotropic X56 steel. As a first step, anisotropy is ignored and the damage model calibration is done using the averaged diameter contraction.

When comparing the experiments to the simulations using the calibrated model, satisfying results were obtained for both steels.

Acknowledgements

The authors acknowledge the support from Research Foundation - Flanders (FWO) via grant G056519N for R. Depraetere and M. Cauwels, while T. Depover holds a senior postdoctoral fellowship of the Research Foundation - Flanders (FWO) via grant 12ZO420N. The authors also acknowledge the in-kind delivery of the X56 steel pipe samples by Gasunie. Further, the authors acknowledge Zhiliang Zhang for providing an implemented version of the complete Gurson model.

References

ASTM E112, 2010. ASTM E112: Standard Test Methods for Determining Average Grain Size. doi:10.1520/E0112-10.1.4.

ASTM E23, 2007. ASTM E23: Standard Test Methods for Notched Bar Impact Testing of Metallic Materials. doi:10.1520/E0023-07AE01.2.

Chu, C.C., Needleman, A., 1980. Void nucleation effects in biaxially stretched sheets. Journal of Engineering Materials and Technology, Transactions of the ASME 102, 249–256. doi:10.1115/1.3224807.

Davis, B.J., 2017. The effect of separations on the assessment of Charpy impact tests. Ph.D. thesis. University of Wollongong.

Gangloff, R.P., Somerday, B.P., 2012. Gaseous hydrogen embrittlement of materials in energy technologies: The problem, its characterisation and effects on particular alloy classes. Woodhead Publishing Limited. doi:10.2307/2524560.

H2Europe, 2020. Hydrogen Europe. URL: https://hydrogeneurope.eu/.

Haskel, H.L., Pauletti, E., Martins, J.D.P., De Carvalho, A.L.M., 2014. Microstructure and microtexture assessment of delamination phenomena in charpy impact tested specimens. Materials Research 17, 1238–1250. doi:10.1590/1516-1439.268314.

Hill, R., 1998. The Mathematical Theory of Plasticity. Oxford classic texts in the physical sciences, Clarendon Press. URL: https://books.google.be/books?id=Wy{_}kuQZzfdIC.

ISO 6892-1, 2016. ISO 6892-1:2016 Metallic materials - Tensile testing Part 1: Method of test at room temperature.

Kim, J.S., Larrosa, N.O., Horn, A.J., Kim, Y.J., Ainsworth, R.A., 2018. Notch bluntness effects on fracture toughness of a modified S690 steel at 150 °C. Engineering Fracture Mechanics 188, 250–267. URL: http://dx.doi.org/10.1016/j.engfracmech.2017.05.047, doi:10.1016/j.engfracmech.2017.05.047.

Oh, C.K., Kim, Y.J., Baek, J.H., Kim, Y.P., Kim, W., 2007. A phenomenological model of ductile fracture for API X65 steel. International Journal of Mechanical Sciences 49, 1399–1412. doi:10.1016/j.ijmecsci.2007.03.008.

Rahimidehgolan, F., Majzoobi, G., Alinejad, F., Sola, J.F., 2017. Determination of the constants of GTN damage model using experiment, polynomial regression and kriging methods. Applied Sciences (Switzerland) 7, 1179. doi:10.3390/app7111179.

Rivalin, F., Besson, J., Pineau, A., Di Fant, M., 2001. Ductile tearing of pipeline-steel wide plates. Engineering Fracture Mechanics 68, 347–364. doi:10.1016/s0013-7944(00)00108-9.

Ruggieri, C., Hippert Jr., E., 2015. Delamination effects on fracture behavior of a pipeline steel: Anumerical investigation of 3-D crack front fields and constraint. International Journal of Pressure Vessels and Piping 128, 18–35. URL: http://dx.doi.org/10.1016/j.ijpvp.2015.01.004, doi:10.1016/j.ijpvp.2015.01.004.

Su, L., Xu, J., Song, W., Chu, L., Gao, H., Li, P., Berto, F., 2020. Numerical investigation of strength mismatch effect on ductile crack growth resistance in welding pipe. Applied Sciences (Switzerland) 10. doi:10.3390/app10041374.

Younise, B., Rakin, M., Gubeljak, N., Medjo, B., Sedmak, A., 2017. Effect of material heterogeneity and constraint conditions on ductile fracture resistance of welded joint zones - Micromechanical assessment. Engineering Failure Analysis 82, 435–445. URL: http://dx.doi.org/10.1016/j.engfailanal.2017.08.006, doi:10.1016/j.engfailanal.2017.08.006.

Zhang, Z.L., Thaulow, C., Ødegård, J., 2000. Complete Gurson model approach for ductile fracture. Engineering Fracture Mechanics 67, 155–168. doi:10.1016/S0013-7944(00)00055-2.